The Meteoritical Society

Meteoritics & Planetary Science 43, Nr 1/2, 415–429 (2008)
Abstract available online at http://meteoritics.org

Discovery of non-random spatial distribution of impacts in the Stardust cometary collector

Andrew J. WESTPHAL[1*], Ronald K. BASTIEN[2], Janet BORG[3], John BRIDGES[4], Donald E. BROWNLEE[5], Mark J. BURCHELL[6], Andrew F. CHENG[7], Benton C. CLARK[8], Zahia DJOUADI[3], Christine FLOSS[9], Ian FRANCHI[4], Zack GAINSFORTH[1], Giles GRAHAM[10], Simon F. GREEN[4], Philipp R. HECK[11], Mihaly HORÁNYI[12], Peter HOPPE[11], Friedrich P. HÖRZ[2], Joachim HUTH[11], Anton KEARSLEY[13], Hugues LEROUX[14], Kuljeet MARHAS[9], Keiko NAKAMURA-MESSENGER[2], Scott A. SANDFORD[15], Thomas H. SEE[2], Frank J. STADERMANN[9], Nick E. TESLICH[10], Samuel TSITRIN[1], Jack L. WARREN[2], Penelope J. WOZNIAKIEWICZ[13, 16], and Michael E. ZOLENSKY[2]

[1]Space Sciences Laboratory, University of California at Berkeley, Berkeley, California 94720, USA
[2]KT NASA Johnson Space Center, Houston, Texas 77058, USA
[3]Institut d'Astrophysique Spatiale (IAS), CNRS, Université Paris-Sud, UMR8617, F-91405 Orsay-Cedex, France
[4]PSSRI, Open University, Milton Keynes MK7 6AA, UK
[5]Astronomy Department, University of Washington, Seattle, Washington 98195, USA
[6]School of Physical Sciences, Room 119, Ingram Building, University of Kent, Canterbury, Kent CT2 7NH, UK
[7]Johns Hopkins University Applied Physics Laboratory, 11100 Johns Hopkins Road, Laurel, Maryland 20723, USA
[8]Lockheed Martin Corporation, Littleton, Colorado, USA
[9]Laboratory for Space Sciences and Physics Department, Washington University, Saint Louis, Missouri 63130, USA
[10]IGPP, Lawrence Livermore National Laboratory, 7000 East Avenue, L-413, Livermore, California 94550, USA
[11]Max-Plank-Institut für Chemie, P.O. Box 3060, D-55020 Mainz, Germany
[12]Laboratory for Atmospheric and Space Physics and Department of Physics, University of Colorado, Boulder, Colorado 80309–0392, USA
[13]IARC, Department of Mineralogy, The Natural History Museum, London SW7 5BD, UK
[14]Laboratoire de Structure et Propriétés de l'Etat Solide UMR 8008, Université des Sciences et Technologies de Lille, F-59655 Villeneuve d'Ascq, France
[15]Astrophysics Branch, Mail Stop 245-6, NASA-Ames Research Center, Moffett Field, California 94035, USA
[16]IARC, Department of Earth Science and Engineering, Imperial College London, South Kensington Campus, London SW11 3RA, UK
*Corresponding author. E-mail: westphal@ssl.berkeley.edu

(Submitted 08 December 2006; revision accepted 24 April 2007)

Abstract–We report the discovery that impacts in the Stardust cometary collector are not distributed randomly in the collecting media, but appear to be clustered on scales smaller than ~10 cm. We also report the discovery of at least two populations of oblique tracks. We evaluate several hypotheses that could explain the observations. No hypothesis is consistent with all the observations, but the preponderance of evidence points toward at least one impact on the central Whipple shield of the spacecraft as the origin of both clustering and low-angle oblique tracks. High-angle oblique tracks unambiguously originate from a non-cometary impact on the spacecraft bus just forward of the collector.

INTRODUCTION

On January 2, 2004, the Stardust spacecraft encountered the comet 81P/Wild 2 at 1.86 AU from the sun at a relative speed of 6.12 km s^{-1} (Brownlee et al. 2004). The distance of closest approach to the comet nucleus was 236 km, on the sunward side. An onboard Dust Flux Monitor Instrument (DFMI) recorded thousands of impacts during two main bursts of comparable fluence (Tuzzolino et al. 2004). The first burst was ~3 min long and was centered on the time of closest approach. The second burst was 1.5 min long and began about 10 min after closest approach. The sample collection tray assembly, consisting of aerogel cells and aluminum foils, was deployed during the encounter to capture cometary particles. The Stardust cometary collector comprised 132 aerogel tiles and 287 aluminum foils, with total collecting areas of ~1039 cm^2 and ~152 cm^2 respectively (Tsou et al. 2003). On January 15, 2006, the Sample Return Capsule (SRC) returned

© The Meteoritical Society, 2008. Printed in USA.

to Earth and was successfully recovered. During the Stardust Preliminary Examination (PE), we optically scanned 132 tiles and 287 foils from which the data discussed here originate. In addition, we did systematic high-magnification surveys by scanning electron microscopy (SEM) on twelve pieces of foils and detailed optical microscope investigations on five harvested aerogel tiles.

The organization of this paper is as follows. In the Spatial Distributions of Impacts in the Stardust Collector section, we report our observations of the spatial distributions of impacts in the Stardust collector and our statistical analysis of these distributions. In the Trajectory Measurements of Tracks in Aerogel in Five Tiles section, we report the trajectory measurements of tracks in five aerogel tiles. In the Crater and Track Residue Compositional Constraints section, we summarize the results of the chemical and mineralogical analyses of residues in craters and tracks. In the Discrepancy between Size Distributions from DFMI and Crater Observations section, we compare the dust fluence measurements derived from the DFMI and from measurements of crater diameters in Stardust Al foils. In the Discussion section, we discuss the consistency of several hypotheses with the observations. Finally, in the Summary section, we summarize and conclude.

SPATIAL DISTRIBUTIONS OF IMPACTS IN THE STARDUST COLLECTOR

Observations

During the course of the preliminary examination, we did surveys to determine the spatial distribution of impacts in the aerogel cells and foils; see Tsou et al. (2003) for details of the collector design. These surveys resulted in four sets of data: complete low-magnification photographic surveys of impacts in aerogel cells and foils on the entire cometary tray, high-magnification surveys of four extracted aerogel tiles, all by optical microscopy, and very high-magnification surveys of twelve aluminum foils by SEM. We also measured the trajectories of 60 tracks in five aerogel tiles. Independently of these observations, we considered in situ observations of dust impacts during the cometary encounter by the DFMI, and measurements of the compositions of track and crater residues. Here we summarize the observations.

Low-Magnification Survey of Impacts in Aerogel and Foils

Using a low-magnification microscope in reflection mode, we recorded digital images of every aerogel tile in the cometary tray and assembled these images into photomosaics. In order to maintain a consistent selection bias, we surveyed these images and recorded sizes and coordinates of 257 impact tracks. The threshold detection diameter for aerogel tracks was 100 μm.

Independently, we surveyed the foils for craters using the same microscope, recording the sizes and positions of each crater. In all, 64 craters >20 μm were found. Because of the very different visibilities of impacts in the two media, the detection thresholds are quite different, and we did not combine the two data sets. In the analysis described below, we considered only impacts into the aerogel tiles.

Whole-Tile Analysis of Normal Tracks

Four tiles that were extracted from the Stardust cometary tray were completely scanned by us using high-magnification microscopy with transmitted illumination. Transmitted illumination enabled orientation to be estimated. These tiles (9, 27, 44, and 115) contained 4, 15, 8, and 9 apparently normal-incidence (<<5°) tracks, respectively. Tile 9 also contained a large number (~100) of very small tracks that entered the aerogel at a significant angle (~8–11°) to the tile normal.

Small Craters in Foils

As part of the "cratering" PE subteam effort, we surveyed all removed foils using SEM at a magnification allowing identification of all craters down to a size of <2 μm. In a second step, randomly selected regions of twelve foils were scanned by high-magnification SEM, allowing identification of craters down to ~100 nm in size. First results are summarized in Hörz et al. (2007) and will be presented in more detail in Green et al. (unpublished data) and Kearsley et al. (2008).

In Table 1, we report the crater surface densities as derived from these surveys, with minimum crater sizes at 350 nm, 1 μm, and 2 μm. The crater density varies between foils by more than a factor of 200 (>350 nm), 50 (>1 μm), and 20 (>2 μm), taking into account the 1σ errors. In Fig. 1, we show a graphical summary of the survey data.

Clustering Analysis

Whole-Collector Analysis of Tracks in Aerogel

A casual inspection of Fig. 1 shows hints of non-random distributions. For example, the two largest tracks in the collection are about 30 mm apart. However, such a coincidence—considered in isolation—is reasonably probable, about 2%.

In order to test rigorously for randomness in the spatial distribution of tracks in aerogel, we considered three statistical tools. The choice of tool was motivated by the nature of the question that we chose to ask: is there a small population of tightly clustered impacts superimposed on a larger randomly distributed population? (Are there "weak clusters"?)

The first is a tool commonly used in cosmology, the two-point correlation function (2PCF) (Davis and Peebles 1983). The 2PCF, $\hat{\xi}$, is a measure of the excess probability of finding neighbors as a function of separation distance r:

Table 1. Summary of small crater observations, including 1σ confidence limits on the fluence. Confidence limits for small statistics were calculated using the tables of Gehrels (1986).

Foil_group	Area scanned (mm^2)	Crater count (>350 nm)	Fluence (mm^{-2}) (>350 nm)	Crater count (>1 μm)	fluence (mm^{-2}) (>1 μm)	Crater count (>2 μm)	Fluence (mm^{-2}) (>2 μm)
20W_Borg et al.	21.4			18	0.84 ± 0.20	12	0.56 ± 0.16
20Whr_	2.62	39	14.9 ± 2.4	10	3.8 ± 1.2	2	$0.7^{+0.9}_{-0.4}$
68W_	18.3	15	0.82 ± 0.21	5	$0.27^{+0.19}_{-0.12}$	0	<0.1
92N_	41	3	$0.07^{+0.07}_{-0.04}$	1	$0.24^{+0.057}_{-0.20}$	1	$0.24^{+0.57}_{-0.20}$
114N_	54	3	$0.06^{+0.05}_{-0.03}$	3	$0.06^{+0.05}_{-0.03}$	0	<0.03
43N_	56	2	$0.036^{+0.047}_{-0.023}$	2	$0.036^{+0.047}_{-0.023}$	0	<0.03
100N_Graham et al.	5	9	1.8 ± 0.6	0	<0.36	0	<0.36
8N_Green et al.	48					35	0.73 ± 0.12
8Nhr_	5			27	5.4 ± 1.0	5	$1.00^{+0.7}_{-0.4}$
125N_	55					3	$0.06^{+0.05}_{-0.03}$
125Nhr_	5			0	<0.36	0	<0.36
54N_	36.4					4	$0.11^{+0.09}_{-0.05}$
54Nhr_	5			5	$1.0^{+0.7}_{-0.4}$	2	$0.4^{+0.5}_{-0.3}$
60W_	18					1	$0.056^{+0.13}$
60Whr_	5			1	$0.20^{+0.46}_{-0.17}$	0	<0.36
51N_	48					1	$0.021^{+0.048}$
37N_Hoppe et al.	1.42	34	24 ± 4	3	$2.1^{+2.0}_{-1.2}$	0	<1.3
44W_	5.5	10	1.8 ± 0.6	0	<0.03	0	<0.03
52N_	9.0	101	11.2 ± 1.1	8	0.89 ± 0.31	0	<0.20
126W_	5.2	1	$0.19^{+0.44}_{-0.16}$	0	<0.35	0	<0.35
44N_Stadermann et al.	5.34	26	4.9 ± 1.0	2	$0.37^{+0.47}_{-0.24}$	0	<0.34

$$\xi(r, \Delta) = \frac{\sum_{\text{pairs}} \phi(d_{\text{obs}}, r, \Delta)}{\sum_{\text{pairs}} \phi(d_{\text{MC}}, r, \Delta)} - 1$$

where $\phi(d, r, \Delta) = 1$ if $r < d < r + \Delta$, otherwise 0. Here d_{obs} is the separation distances of the $N(N-1)/2$ unique pairs among the N impacts in the data set, d_{MC} is the pair-wise separation distances of randomly placed impacts over the same fiducial area, and Δ is the bin width.

The second statistical tool was a single statistic $\hat{\xi}$. ζ is defined as:

$$\zeta = \log \sum_{\text{pairs}} \frac{1}{d^2_{\text{pair}}}$$

where d_{pair} is the separation distance of each pair, and the sum is taken over the $N(N-1)/2$ unique pairs among the N tracks in the fiducial region. $\hat{\zeta} = \zeta - \langle\zeta_{\text{MC}}\rangle$, where $\langle\zeta_{\text{MC}}\rangle$ is the average value of ζ for a large ensemble of Monte Carlo simulations of N randomly positioned events on the tile. $\langle\zeta_{\text{MC}}\rangle$ and the error bars were determined by running 10,000 Monte Carlo simulations.

Finally, we considered a standard technique in cratering analysis, mean nearest neighbor analysis (MNNA) (Squyres et al. 1997).

We evaluated all three techniques (2PCF, $\hat{\zeta}$, and MNNA) using a randomly generated data set consisting of 232 tracks randomly distributed over the tray and with an additional 25 tracks randomly distributed within a quarter of one tile. We found that 2PCF and $\hat{\zeta}$ both showed very highly significant deviations from random distributions, but that, somewhat surprisingly, MNNA was insensitive to the presence of the cluster, showing <1σ deviation from random. We concluded that MNNA is not well-suited for testing for weak clustering analysis.

Figure 2 shows the 2PCF for the distribution of tracks in aerogel. The error bars were determined using 10,000 Monte Carlo simulations of randomly distributed tracks in the aerogel tiles in the tray. A random distribution gives, within errors, a flat distribution at $\hat{\xi} = 0$. The 2PCF shows a significant (2.8σ) excess probability of about 10% at the smallest scale (less than ~50 mm), with weaker evidence of a deficit at the scales larger than ~20 cm.

To test whether the clustering might be due to a specific size range, we progressively removed small tracks from the data set. We chose to look at the bin with the largest $\hat{\xi}$ value, $\hat{\xi}_1$, in the bin centered on 30 mm in Fig. 2. We divided the data set into deciles, then removed first the smallest 10%, the smallest 20%, and so on. The largest statistical excess (2.8σ) in the 2PCF is shown by the entire data set, but the excess does not appear to decrease significantly with increasing minimum particle size.

We also evaluated the data set using the $\hat{\zeta}$ statistic. Again, we removed the smallest tracks in deciles. The results

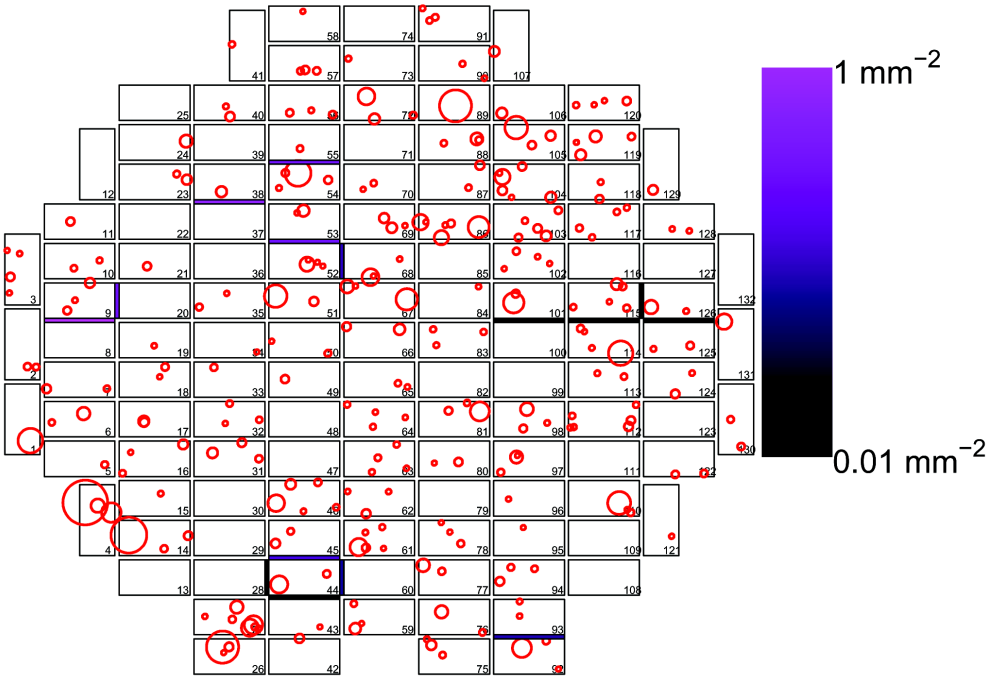

Fig. 1. Schematic diagram of the Stardust cometary collector. Tracks in aerogel are shown as circles, with the diameters of the circles proportional to the square root of the maximum throat diameter of the particle track. The largest track, at the lower left in tile 4, is 9.96 mm in diameter. Crater densities in foils are also shown in false color, according to the legend at right. Foils with no detected craters are shown as black, even if the upper limit on the fluence is greater than 0.01 mm^{-2}. The numbers are the official tile numbers. "N" and "W" foils are adjacent (north and west) to the aerogel cells with the same name. Aerogel tiles measure 2 cm × 4 cm.

are shown in Fig. 3. We find evidence that the smallest 10% of tracks are responsible for the statistical excess (2.4σ) in $\hat{\zeta}$. There is also a marginal statistical excess (2.0σ) for tracks larger than ~300 μm.

Whole-Tile Analysis of Tracks in Aerogel

The tiles that we analyzed, 9, 27, 44, and 115, contained at most 15 normal-incidence tracks. For such small track statistics, the 2PCF is not useful as a statistical measure, so we used the $\hat{\zeta}$ statistic only.

Only one of the four tiles, tile 27, showed significant evidence of clustering (Fig. 4).

In Fig. 5, we show a map of the track locations in tile 27. This tile contains two large, nearly identical impacts that are only ~3 mm apart, near three other tracks. The tracks analyzed in tile 27 include both large and small particles. As mentioned above, tile 9 contained numerous off-normal tracks. These tracks were not included in the clustering analysis described here. Unfortunately, the tracks in tile 27 were extracted for analysis before their trajectories could be analyzed.

Clustering analysis of the Al foil crater data. Because of the limited statistics—due to small fluence—in some of the foils, 2PCF analysis was not appropriate for this data set. Because detection thresholds among the various groups varied, we did not mix data sets from different groups when evaluating clustering.

We analyzed the spatial distribution of small craters using the same sum-inverse-square statistic $\hat{\zeta}$ that we used for the analysis of tracks in individual aerogel tiles (Fig. 6). Out of 22 scan regions on ten foils, five showed significant (>2σ) evidence for non-random spatial distributions. For this analysis, we used all craters detected, not just the craters >350 nm in size shown in Table 1.

During the course of surveying foil 8N, the Open University group discovered a spectacular cluster of 37 craters contained in an approximately 20 μm × 20 μm area (Fig. 7). In this analysis, this cluster was counted as only one crater. If the components of the cluster been counted individually, the statistical significance for clustering would have been unmeasurably high (>>5σ) by Monte Carlo methods.

Summary of Clustering Analysis

Small craters in the foils are clustered at a statistically significant level. 2PCF and $\hat{\zeta}$ analyses of the spatial distribution of tracks in aerogel also show evidence of weak clustering, although the statistical significance is somewhat smaller. The two analyses show different behaviors as a function of minimum aerogel track size. The 2PCF analysis indicates that ~10% of tracks are clustered.

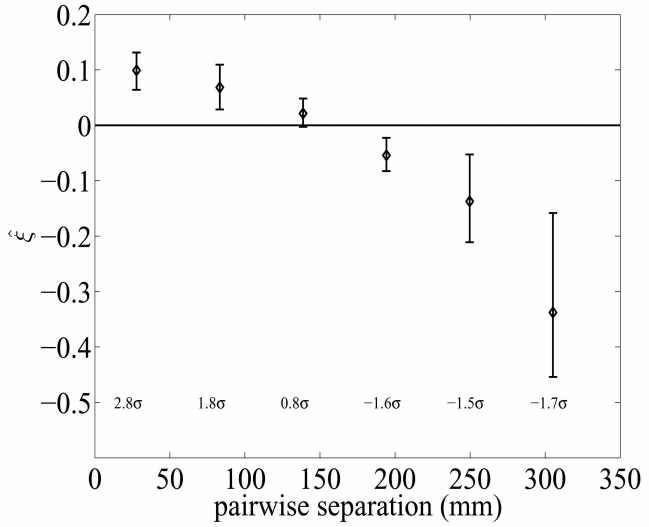

Fig. 2. The two-point correlation function $\hat{\xi}$ plotted versus track separation. The statistical significance of the departure from random ($\hat{\xi} = 0$) is given for each point.

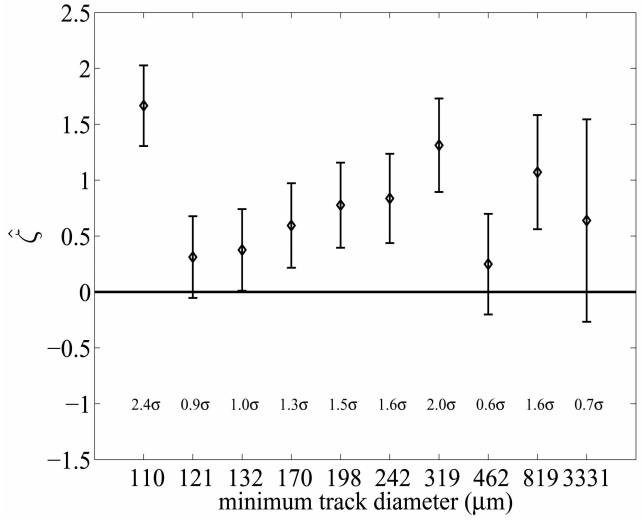

Fig. 3. $\hat{\zeta}$ versus minimum particle size.

TRAJECTORY MEASUREMENTS OF TRACKS IN AEROGEL IN FIVE TILES

During our survey, we observed in tile 9 a large population of nearly parallel tracks that deviated significantly from normal incidence, the nominal trajectory of Wild 2 particles. We thus measured track orientation (zenith and azimuth angles) for a number of tracks in aerogel tiles 9, 38, 44, 52, and 86, using an optical microscope with an encoded stage (0.5 μm resolution). We used a least-squares fit to estimate the trajectory of the tracks before impact with the aerogel. We excluded the bottom portions of tracks except on extremely small impacts (<200 μm deep). This was necessary because large (>200 μm deep) hypervelocity particles often veer as they transition into the subsonic domain. By contrast, those with depths less than ~200 μm were found to have correlated trajectories and were assumed therefore not to veer randomly after impact. Because the off-normal tracks were so numerous in tile 9, we did not select tracks randomly, but instead selected arbitrary regions and included all tracks within those regions.

In Fig. 8 we show a side view of the Stardust spacecraft. We projected the trajectories onto the plane of the central Whipple shield that protected the front of the spacecraft bus to evaluate the possibility that they may have originated from a collision between a cometary particle and the edge of the shield (Fig. 9). Of the tracks measured, 39 are consistent with primary, normal-incidence impacts, and 21 cross the plane of the Whipple shield at or below the bottom edge of the collector (below –20 cm). No projected trajectories crossed the plane of the Whipple shield above the projected top of the collector.

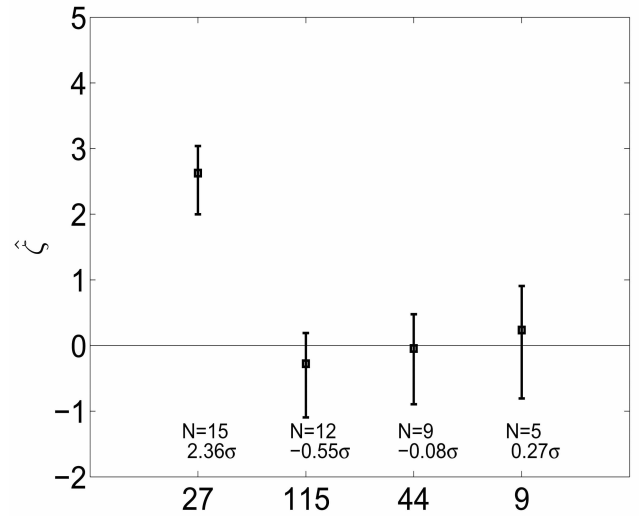

Fig. 4. $\hat{\zeta}$ for the tiles 9, 27, 44 and 115. A random distribution of track positions corresponds to $\hat{\zeta} = 0$. The distributions are asymmetric and non-Gaussian, so the confidence level, expressed in units of s, is listed for each tile.

The presence of a significant population of particles coming from below the bottom edge of the collector suggests the existence of secondary ejecta from the Whipple shield. However, we cannot exclude the possibility that the off-normal population is a population of dust with a large radial velocity component with respect to the Wild 2 nucleus (~1 km sec^{-1}) that marginally misses the Whipple shield. We discuss this possibility further below.

In addition, several clusters of tracks had both high incidence angles and correlated trajectories. One of these clusters on tile 9 had four tracks within a 1 mm^2 area, and their

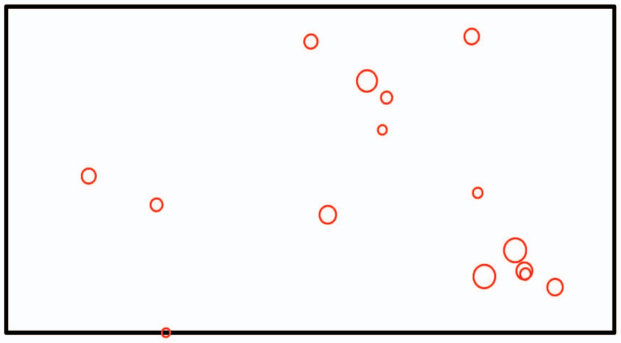

Fig. 5. Map of tracks in aerogel tile 27. The diameter of the circles indicates the maximum diameter of the particle track in the aerogel, but is exaggerated by a factor of 10 in this figure. The aerogel tile measures 2 cm × 4 cm.

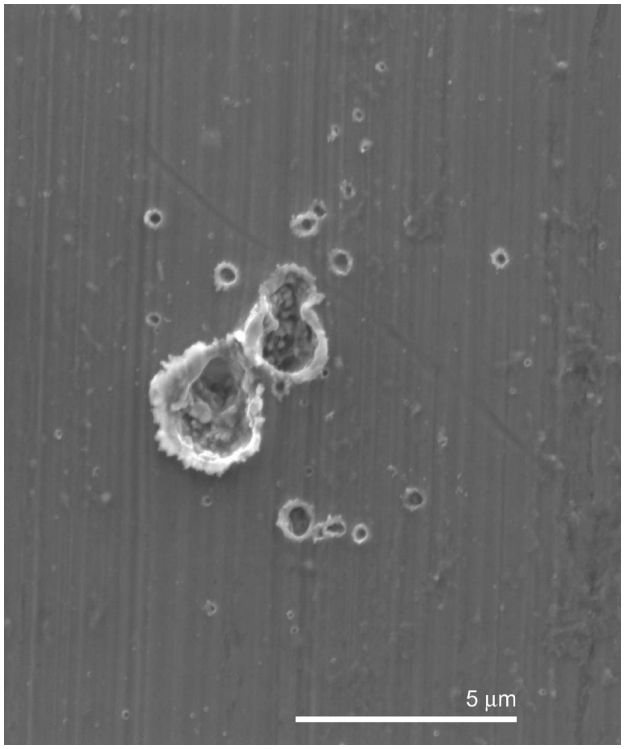

Fig. 7. A cluster of 37 craters in foil 8N, discovered and imaged by the OU group. The craters are distributed over 350 µm^2.

trajectories projected toward the center edge of the Whipple shield. This suggests that particles with a high incidence angle are clustered.

We observed that off-normal tracks systematically exhibit a morphology distinct from the morphologies of normal tracks. Off-normal tracks generally lack a distinct bulb (tracks of type "A" (Burchell et al. 2008), while normal-incidence tracks are highly variable. We did no extensive systematic study of this phenomenon.

In the course of scanning tile 44, we also discovered a population of highly oblique tracks, ~70° (Fig. 10). Their

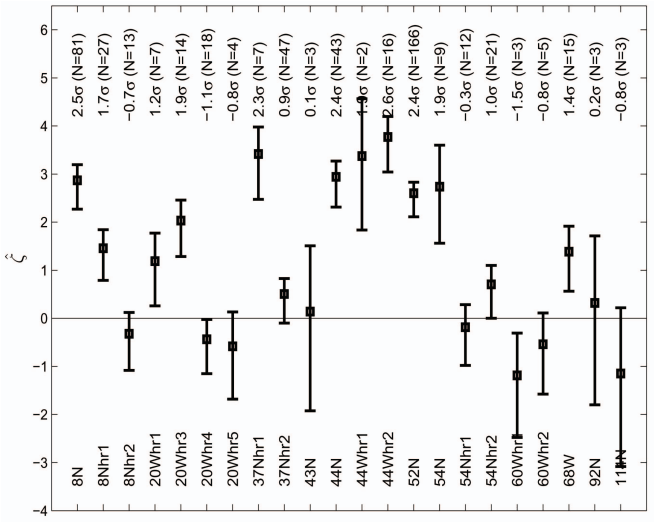

Fig. 6. $\hat{\zeta}$ for 22 foil surveys. A random distribution of crater positions corresponds to $\hat{\zeta} = 0$. The distributions are asymmetric and non-Gaussian, so the confidence level, expressed in units of σ, is listed for each foil. This crater cluster in 8N, shown in Fig. 7, was treated as one crater in this analysis. The suffixes "r1" to "r5" refer to different regions of the same foil.

trajectories are consistent with an origin in ejecta from an impact on the spacecraft bus just below and forward of the collecting tray.

CRATER AND TRACK RESIDUE COMPOSITIONAL CONSTRAINTS

A detailed mineralogical and compositional analysis of numerous impactor residues in the interior of craters and tracks was conducted during Stardust PE. None of the tracks provided conclusive evidence that collisionally dislodged spacecraft materials contributed to the impact features seen on Stardust's cometary collector. Specifically, the cratering group (Hörz et al. 2007) analyzed the melt residues of some 200 craters <5 µm in diameter via SEM-EDS methods, including features in exceptionally close proximity to each other that appeared to be part of a non-random impactor population. Also, some 38 individual craters composing the specific cluster illustrated in Fig. 7 were investigated by Bridges et al. (unpublished data), all yielding impactor residues consistent with cometary grains, and akin to those observed in the suite of 200 craters. Six large craters (>40 µm) were analyzed in detail via SEM-EDS (Kearsley et al. 2007) and TOF-SIMS (Leitner et al. 2008), none yielding compositions compatible with spacecraft materials.

Considering the ease with which natural and manmade impactors can be distinguished on space-exposed surfaces retrieved from low Earth orbit (Levine et al. 1993), the Stardust crater observations suggest little to no collector contamination by spacecraft materials. It is noted, however,

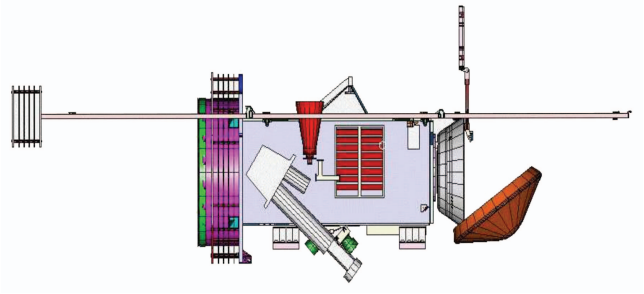

Fig. 8. Side view of the Stardust spacecraft.

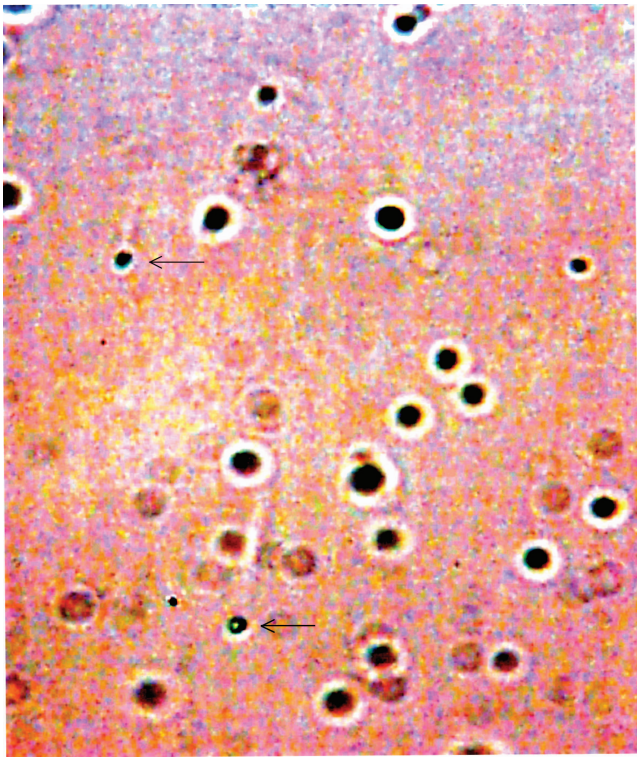

Fig. 10. High-contrast image of highly-oblique secondary tracks. The field of view measures 51 μm × 67 μm.

that the suite of craters <5 μm in diameter included a few features (<2%) of indeterminate projectile composition; these features most likely contained residue masses below the detection threshold of the SEM-EDS method. It is possible also that they were produced by either aluminum or Kapton particles; Al impactors can obviously not be resolved from the Al-collector background, nor is the SEM-EDS method sensitive to small quantities of organic materials composed of low-Z elements. Analysis of numerous Stardust surfaces, however, does not reveal the presence of Kapton among the many organic contaminants, nor was Kapton observed in any of the tracks analyzed for organic components based on (Sandford et al. 2006).

Additionally, a total of 27 tracks were analyzed via high-energy, synchrotron-produced, X-ray beams, yielding

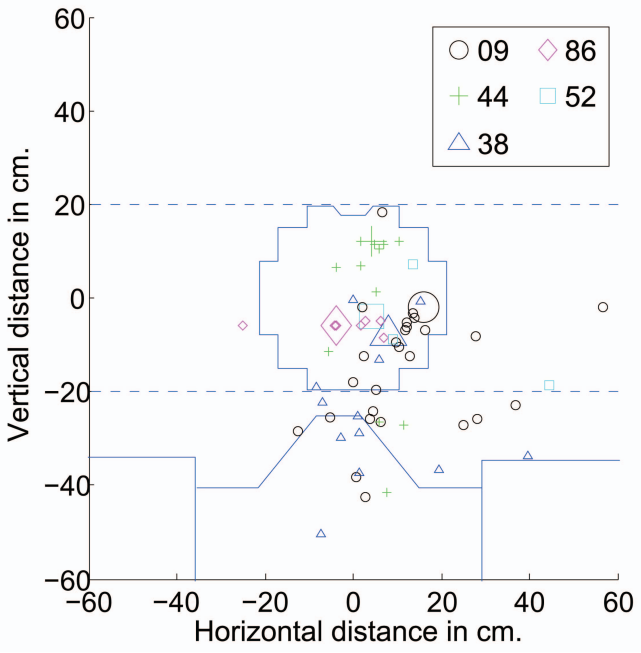

Fig. 9. Aerogel tracks projected onto the plane of the central Whipple shield. The spacecraft bus is at the bottom of the picture. The Wild 2 nucleus passed below the spacecraft. The Whipple shield outline is shown at –40 cm on the y axis and includes the trapezoidal protrusion. The rectangular Whipple shields to each side are the solar panel shields and are located in a different plane. Parallax between the solar Whipple shields and the impact sites has been ignored for readability. The outline of the collector is shown at the center. Symbols indicate the tile of origin; the tiles are the magnified symbols.

detailed elemental X-ray fluorescence maps of the impactor materials along the entire penetration path (Flynn et al. 2006). These analyses illustrate distinctly lumpy distribution of elements, consistent with 1) the generation of numerous submicron particles as the impactor penetrated, and 2) the preservation of relatively large particles at the terminus of individual tracks. None of these individual particles, large or small, yields evidence for spacecraft derived origins. (We note that synchrotron X-ray fluorescence analysis is insensitive to elements with Z <16.) This is corroborated by quantitative TEM investigations of some 300–400 individual particles in 52 individual Stardust tracks (Zolensky et al. 2006), all yielding predominantly natural comet materials. However, some rare particles rich in Ti, Au, and Zr were observed and their origin is currently unresolved; although they seem anthropogenic, they do not necessarily represent materials collisionally dislodged from some spacecraft surface, as none of them were detected as crater residue. They also seem too infrequent to be the main source of the common and numerous non-random impacts on the collector.

In summary, detailed compositional analysis of Stardust craters and tracks provides no evidence for a prominent collisional environment by spacecraft debris.

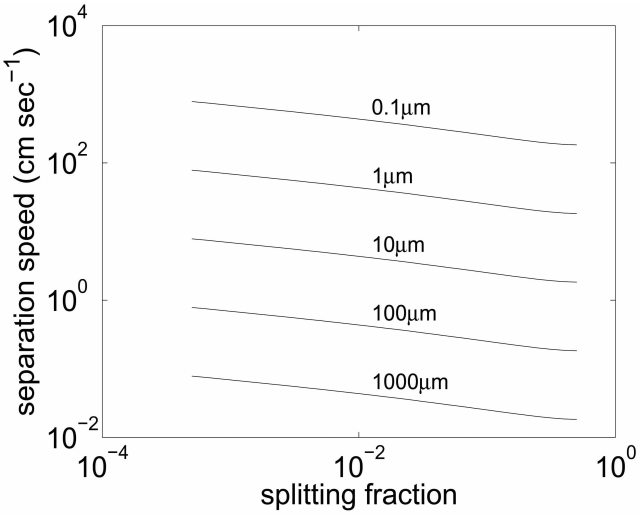

Fig. 11. Separation velocity of fissioning dust particles with a potential of 1V, as a function of the fraction of the smaller daughter's mass compared with that of the parent. Each curve is labeled with the radius of the parent particle. Particles are assumed to be spheres with density 1.0 g cm^{-3}. Here we assume that during fission, charge is partitioned between the daughter fragments in proportion to their surface area. The separation velocity increases linearly with electric potential.

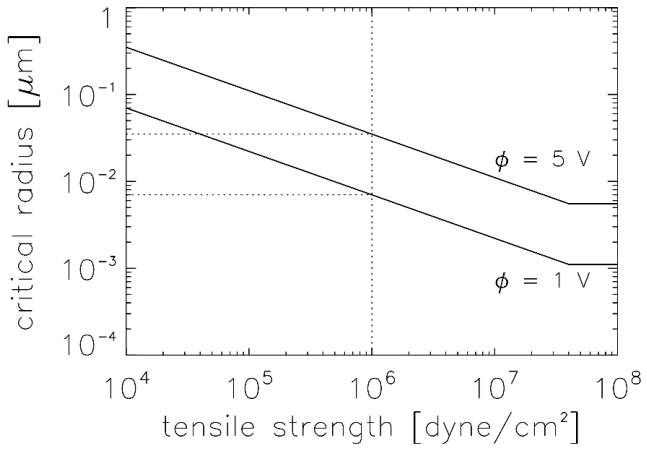

Fig. 12. Critical radius of grains as function of the tensile strength. Grain smaller than the critical size are unstable against electrostatic disruption. The break is due to the field emission limit.

DISCREPANCY BETWEEN SIZE DISTRIBUTIONS FROM DFMI AND CRATER OBSERVATIONS

Two measurements of the dust fluence and size-frequency distribution from the Stardust Wild 2 encounter have been reported. The Dust Flux Monitor Instrument (DFMI) measured the masses of impacting cometary dust in situ during the cometary encounter, using a combination of PVDF thin film sensors (for diameters a > ~3 μm) and piezo-electric acoustic sensors (for a > ~50 mm) (Green et al. 2004; Tuzzolino et al. 2004; Hörz et al. 2007) reported dust fluence and size-frequency distributions as derived from measurements of individual crater diameters in the Stardust cometary-collector aluminum foils, as well as in aerogel. The measurements are strongly inconsistent, both in absolute fluence and in their spectral mass index, α. The disagreement is in the PVDF data, which show α ~ –0.85. The acoustic data, which agree in fluence with the foil data in the overlap region around grain radius of 50 μm, have a lower average slope (α = –0.5) and fluences that are exactly coincident with that derived from the large craters. Despite considerable effort, neither group has been able to identify any technical problem with either technique that resolves the discrepancy.

We point out that a scenario exists that could resolve the discrepancy. A population of small dust grains with a large radial velocity (>1.4 km s^{-1}) with respect to the Wild2 nucleus would be detected by DFMI because of its position on the nose of the spacecraft. We discuss expected ejection velocities of cometary dust in the Dispersion Speed of Disintegrating Dust section. Because of shadowing by the spacecraft bus, this population would pass over the collector, missing it entirely. A population of dust with a somewhat slower velocity, ~1 km s^{-1}, could be consistent with the off-normal tracks that we observe. However, this shadowing effect would not operate during the second dust collection period, ~4000 km downrange of the point of closest approach. We note that the discrepancy between foil and DFMI spectral indices is larger for the second collection period (Green et al. 2004).

DISCUSSION

We consider three general scenarios in seeking to understand the clustering observations: fragmentation processes in the cometary coma, spacecraft-induced fragmentation unrelated to impacts, and fragmentation due to one or more impacts on the spacecraft.

Processes in the Cometary Coma

It is natural to expect that, after they are ejected from the comet nucleus, cometary dust particles spontaneously fragment as they are heated by the sun and any remaining volatile "glue" holding them together sublimes away. Fragmentation of larger aggregates released from the Wild 2 nucleus was inferred to explain the highly variable fluxes detected on subkilometer to kilometer scales in the in situ DFMI data (Tuzzolino et al. 2004; Green et al. 2004). A number of possible modes of fragmentation, physical mechanisms, and observational evidence from other comets were discussed by Clark et al. 2004.

Fragmentation of larger aggregates released from the Wild 2 nucleus was detected as relatively large-scale (subkilometer to kilometer) clustering (Clark et al. 2004).

However, three especially tight clusters account for 33% of all counts observed during the fly-by (Tuzzolino et al. 2004). For each of these, the counts were confined within a single 100 ms DFMI measurement interval, or straddling only two intervals, and with counts in the prior and subsequent measurement intervals 1 to 3 orders of magnitude lower. The first case was at +1.65 s after closest approach. The other two occurred in the late event, ~600 s after fly-by. It cannot be excluded that these three extremely tight clusters actually arrived over an interval significantly smaller than one measurement interval. These could possibly have consisted of multiple subclusters within which the spatial separations between sequential particles were so small that two or more impact events would have been sensed as a single event due to pulse pile-up in the few microseconds signal-processing chain in the DFMI electronics system (Tuzzolino et al. 2003). Thus, these intense clusters of counts could account for an even larger fraction of all events measured by DFMI and the clusters could be more spatially confined than the DFMI data can demonstrate.

Dispersion Speed of Disintegrating Dust

Disaggregation can be most straightforwardly modeled as a gradual loss of material that is volatile under coma conditions of solar illumination and very low pressure. This material is a mixture. Water, CO_2, and numerous other condensates, including high-volatility organic materials, are well-known constituents of the gas phase of cometary comae. In porous aggregates, the sublimation process itself would only very gently separate the non-volatile grains, unless the volatiles are somehow confined such that they can build up pressure before release. Stiction by residual surface material and van der Waals forces would resist immediate disaggregation. However, separation forces have been identified that would promote subsequent breakup. These include centrifugal and electrostatic forces.

The separation between particles at the time of observation depends upon the time since separation and the energetics of the separation process itself. Many generations of breakup are implied by the shapes of the dust size distributions in comae (Clark et al. 2004), and some of the progeny particles may have separated only minutes before observation.

Rotation is inevitable for particles in space. Asymmetric loss of volatiles and solar radiation pressure on albedo variations are driving forces, but simple stochastic variations in solar wind can also induce the particles to tumble. This breakup can be gentle. For example, separation distances between sibling particles from a common progenitor 35 μm in diameter will be less than 1 cm at 1000 s after centrifugal breakup, if the progenitor tumbles at a period greater than 10 s. Smaller particles will produce siblings with even lower separation velocities.

Dust particles ejected from the comet, even if they are initially electrically neutral, become charged to a potential of several volts magnitude through a variety of mechanisms, including photoejection of electrons by solar ultraviolet radiation, producing positive potentials of a few volts, and absorption of fast electrons in the surrounding plasma, producing much larger negative potentials. For 1 μm particles at 1.8 AU, charging requires ~100 s (Horányi 1996); the charging time decreases inversely with increasing particle size. After fragmentation, the daughter fragments repel each other by electrostatic repulsion. In Fig. 11, we show the asymptotic separation speed of the daughter fragments as a function of parent particle mass and splitting fraction. For parent particles 10 μm in size or smaller, asymptotic separation speeds are at least 1 cm s^{-1} or faster. We assume that during fission, charge is partitioned between the daughter fragments in proportion to their surface area. Separation speeds could be significantly lower only if the partition of charge departs dramatically from this assumption. From Fig. 2, we see the strongest evidence for clustering at distances less than 10 cm. For fissioning ~20 μm dust, we estimate a separation speed of order 1 cm s^{-1}, so for these dust particles dispersal must have started no more than 10 s before collection.

We define a parameter, η, which is the fraction of captured particles that belong to clusters with characteristic sizes of 10 cm or smaller. From Fig. 2, $\eta \sim 0.1$. Following Clark et al. (2004), we consider three principle fragmentation modes: shedding, disintegration, and fission.

If particles principally fragment by shedding, in which numerous small particles are released gradually, a fraction η of the captured particles must have been shed within 10 s of the collection time. If the shedding process occurs more or less continuously and smoothly, we then can estimate the characteristic shedding time as $\tau_s = 10\ \text{s}/\eta \sim 100$ s. Similarly, if particles fragment by sudden and catastrophic disintegration, the characteristic disintegration time τ_d is of the same order. Dust particles must travel at least 236 km from the comet nucleus before capture by the spacecraft. This implies a speed significantly greater than 2 km s^{-1}. We exclude this possibility for two reasons. First, as discussed previously, particles travelling radially outward from the comet nucleus at 2 km s^{-1} would be geometrically prevented from reaching the collector over most of the first collection period and over all of the second. Second, it appears to be difficult to eject dust from the comet at such a large speed. At least some dust was probably ejected from Wild 2 by entrainment in gas jets (Sekanina et al. 2004). The gas speed in these jets is unknown, but a strict upper limit can be calculated if it is assumed that these jets are supersonic, as would be the case if they were powered by a pressurized reservoir and there were constrictions near the comet surface (Yelle et al. 2003). The limiting exit velocity of a supersonic nozzle with zero exit pressure is $\sqrt{2/(\gamma-1)}\, c_s$, where γ is the ratio of specific heats and c_s is the sound speed. If the accelerating gas is diatomic, $\gamma = \frac{7}{5}$. The temperature of the comet is no more than ~300 K, so the limiting gas speed is ~0.7 km s^{-1}. (We note that the limiting speed calculated by Yelle et al. [2003], ~3 km/s, appears to be overestimated.) Acceleration of dust grains by an accelerating gas flow depends

on the geometry of the exit channel, but is generally not very efficient at the expected pressures for grains larger than ~1 μm, so the asymptotic speed of the grains is a small fraction of the final gas velocity (Yelle et al. 2003). So it appears that fragmentation principally by shedding or disintegration is not responsible for our observations of clustering.

Next we consider fission, in which particles fall apart stochastically into fragments of comparable size. The characteristic fission time, τ_f, is also of order 100 s for the parents of the particles that were captured. If the progenitor object that was ejected from the comet had a mass m_0 and the characteristic mass of the captured particles was m_f, then the number of generations of fragmentation is $n_g \sim \log_2(m_0/m_f)$. For example, for $m_0 = 1$ g and $m_f = 1$ ng, $n_g \sim 30$. The required radial particle speed is reduced by a factor of n_g; for a 1 g progenitor, this is ~70 m s^{-1}. This is still an unexpectedly large escape speed for such a large object, but in this treatment we assumed that τ_f is a constant, independent of particle size. Although we cannot be quantitative, τ_f should increase dramatically with increasing particle size (Clark et al. 2004); this reduces the required radial particle speed accordingly.

Spacecraft-Induced Fragmentation (Non-Impact)

Did the particles fragment just before capture due to some influence of the spacecraft? We first consider the possibility of a gas-dynamic shock. From astronomical observations of Wild 2, the molecular production rate (Farnham and Schleicher 2005) was about 10^{28} molecules s^{-1}. Gas should not come off any more slowly than the speed of sound, which is around 300 m s^{-1}. By mass balance, the gas density at 236 km is about $<4 \sim 10^7$ cm^{-3} (v/(300 m s^{-1})). The corresponding mean free path is >10 km, which is much larger than the spacecraft, so disruption by a gas-dynamic shock can be ruled out. Another possible source of gas is the spacecraft itself, especially from freshly activated surfaces due to sputtering by incoming particles. We currently have no basis for estimating the importance of spacecraft outgassing.

A charged dust grain will disintegrate if the electrostatic stress exceeds the tensile strength of the grain (Mendis and Rosenberg 1994). While the tensile strength is independent of grain size, the electrostatic stress ~$1/a^2$, hence grains disrupt below a critical radius $a_\mu^c \approx \frac{7|\phi^V|}{\sqrt{F_T}}$, where a_μ^c is measured in μm, and F_T is the tensile strength measured in dyne/cm^2. Typical values for F_T range from 10^4 (dust ball) to 10^{11} (tektites), and it is thought to be on the order of 10^6 for fragile cometary dust particles. The expected floating potential in a cometary environment is a few volts positive. Grains smaller than 70–350 nm will break up, assuming a surface potential of 1–5 V (Fig. 12). The products are even more unstable and continue disrupting until the field-emission limit is reached. Grains with $a_\mu \phi^V / 900$ lose their charge by emitting electrons and will not disrupt. This indicates that if electrostatic disruption is at work, the grouping of grains could be expected in the 1–5 nm range.

Even though electrostatic disruption is likely to take place, it is still difficult to see why these events would take place preferentially in the vicinity of the spacecraft. The close vicinity of the spacecraft is dominated by photoelectrons released from the lit side of the spacecraft, i.e., the side facing away from the nucleus. These photoelectrons have typical energies of 2 eV, so an approaching particle can only start losing its positive charge and—if big enough—can even switch to a negative charge, but just with a floating potential of about −2 V. The sign of the charge has no effect on the electrostatic stress (~E^2). The characteristic charges are expected to be comparable or smaller than the charges in the solar wind. Unless the charging/discharging itself would induce stresses, grains will not be exposed to a harsher electrostatic environment close to the spacecraft.

We have speculated that a large impact on one of the Whipple shields could have produced a cloud of particles, mostly fibers from the Nextel fibers, that could serve as targets for cometary particles, fragmenting them just upstream of the collector. The time-averaged cross section of these fibers upstream of the spacecraft is difficult to estimate. Large ejecta speeds (>>10 m s^{-1}) are observed in test impacts on Whipple shields, so the loitering time of these fibers near the spacecraft is likely to be less than a second.

We consider the possibility that particles could form stable or quasi-stable configurations of spatially separated dust particles. Simpson et al. (1979) have proposed that in some situations grains of different sizes or of different compositions may charge to different signs. In this case, if smaller daughter fragments could quickly acquire a different charge sign than the larger parent after fragmentation, they could reconverge and rejoin the parent. They would then acquire the same charge as the parent by conduction, fragment again, and repeat this process indefinitely. However, the charging time of the smaller daughter fragment appears be too long for this mechanism to be effective (Horányi 1996).

Spacecraft-Induced Fragmentation (Impact)

Whipple Shield as a Target

We now consider the probability that an impact on the central Whipple shield might produce secondary ejecta. These ejecta would appear in the collector as off-normal tracks. The Stardust Whipple shields consisted of two (ram and wake) aluminum honeycomb panels with graphite epoxy facesheets, located on the front and rear of the assembly. Several layers of Nextel ceramic cloth blankets were located between the front and rear honeycomb panels. The shields were covered with multi-layer insulation (MLI) consisting of 13 layers of 6-micron aluminized mylar and dacron nets. This assembly was wrapped with 25–50-micron thick aluminized kapton. The aluminized side of the kapton faced the interior

of the assembly. The kapton was secured to the MLI with 12.5-micron thick tape using an acrylic adhesive. In summary, possible contaminants from the Whipple shield are kapton, acrylic, aluminum, mylar, dacron, graphite, epoxy, and ceramic cloth, in order of required excavation depth from the Whipple shield.

An accurate estimate of the cross section of the rolled edge is probably impossible. If the radius of curvature of the foil as it folds around the edge is 1 mm, then the total cross section is of order a few cm^2, practically independent of spacecraft pitch. The fluence of particles greater than 10 μm in size as estimated from the crater data is ~0.3 cm^{-2} (Hörz et al. 2006), so it is likely that at least one particle >10 μm in size impacted this rolled edge. The obliquity could vary from zero to 90 degrees depending on where the particle(s) hit on the curved surface of the roll.

The top face of the Whipple shield is another potential target. The obliquity of such impacts is likely to be very large—this depends on how taut the kapton was pulled during spacecraft construction. The extent to which wrinkles project above the projected edge of the Whipple shield is unknown. Shallow wrinkles are visible in documentary photographs. But even if the face had been perfectly flat, the cross section would be highly uncertain. If the spacecraft was slightly pitched up, the cross section would be zero. If the spacecraft was slightly pitched down, the cross section could be very large. For example, if the spacecraft was pitched down by even 1 degree, the cross section would be several times that of the front rolled edge.

Trajectories of Projectile and Target Fragments for High-Obliquity Impacts

What is of interest here is the fate of the projectile material and ejecta from the target, which may depart from a primary impact site in front of the aerogel collector tray and which then intercepted the Stardust collector. In general, the ejecta cloud begins to show asymmetries as the angle of incidence deviates from normal incidence. At extreme angles of incidence, the projectile no longer couples fully into the target during the impact. Instead, at the impact point an increasing fraction of it ricochets off projectile's rear surface, a process called impact "decapitation" by Schultz and Gault (1990), which causes the top of the projectile to shear off during impact and strike the target downstream of the primary crater, leading to extensive gauging and elongated crater cavities. At extreme angles, significant fractions of the projectile ricochet off the target surface altogether at some mean angle of rebound. This is in addition to any fine, high-speed spray produced during the initial contact stage of the impact. Thus what are essentially macroscopic fragments of the projectile survive the primary impact and travel away from the primary impact point. In addition, some of the material ejected from the target also travels in a forward direction, accompanying this projectile material.

Gault (1973) observed oblique impacts in dense crystalline rocks (speed 1 to 8 km s^{-1}), showing that the displaced target mass varied with $\sin 2\theta$ (where θ is the angle of incidence measured from the target surface), implying that, for example, at 10° the displaced target mass would only be 3% of that at normal incidence. Impacts in dense crystalline rocks were revisited by, among others, Burchell and Whitehorn (2003) at speeds of 5–6 km s^{-1} and angles of incidence as low as 5°. At 10°, their measured excavated crater mass was 10% of that at normal incidence, and at 5° it was 4%. They found that ejected mass varied as $\sin\theta$, although at shallow angles the measured values were slightly below this dependence. Either way, the total amount of target material ejected is much less than for normal incidence.

Gault and Wedekind (1978) studied oblique, high-speed impacts in non-cohesive quartz and pumice. They reported that the excavated crater mass varied as $\sin\theta$. For shallow angle impacts, they found forbidden azimuthal zones in the ejecta distribution. These zones had bilateral symmetry, extending both up- and down-stream of the primary crater (similar to patterns evident around large craters on the moon). As well as the bulk ejecta from the target, they noted the presence of high-speed ejecta which was impact-melt-removed from the crater very early in the cratering process. At very shallow angles of incidence, this melt ejecta was confined to a very narrow range of azimuth angles in the downrange direction. There was some projectile material in the impact ejecta at all angles of incidence, but as the angle became shallower, this increased and was focused in the forward direction. In all cases, the displaced materials also had very shallow take-off angles in the downrange direction, as detailed below.

There was no single critical angle for the onset of this focusing of the projectile material; it depends which phenomena was used to flag the onset of ricochet. This was commented further on by, e.g., Burchell and Mackay (1998), who found several critical angles in oblique impacts, depending on whether crater shape, appearance of rays on the target surface, etc. were used to flag the onset of this behavior. Most authors note that these angles depend on target and projectile composition as well as impact speed, but that the phenomena of ricocheting projectile material in the forward direction is fully apparent for impact angles 10° to 15° from the target surface. Indeed, for very shallow angles (few degrees), at some speeds and some projectile/target materials, the entire projectile can skip off the surface with no apparent fragmentation and little deformation. In such cases the forward ejecta mass is totally dominated by the projectile. However, Gault and Wedekind (1978) noted that (for non-cohesive targets) even where all large fragments in the downstream forward direction appeared to be projectile fragments, there was still a very fine-sized population of target material. For the ricocheting projectile fragments, Gault and Wedekind (1978) found no simple relation between

angle of incidence and angle of ricochet. At 6.1 km s^{-1}, they observed that for angles of incidence of 2°–7°, the ricochet angle was between 0.75° and 1.1° with the speed of the ricocheting fragments some 80–90% of the impact speed. In Gault and Schultz (1986), similar experiments on granular targets were repeated, but with the addition that the history of target ejecta was also considered. They found that for impacts at 7.5°, the projectile fragmented with a mean velocity after ricochet of 82% of the pre-impact speed, and the projectile fragments were accompanied by target material equivalent to 27% of the projectile mass.

Highly oblique incidence impacts in space have been determined as the origin of the loss of imaging capability on X-ray telescopes in Earth orbit. These possess long mirrors that are highly inclined to the direction of the incidence radiation; these act to focus the very short wavelength X-rays. Laboratory studies (Meidinger et al. 2003) using micron-sized iron projectiles at angles of incidence of 1–2° and speeds of 5.0 ± 0.5 km s^{-1}) have shown that these surfaces also focus ejecta (from highly oblique dust impacts) onto the CCD cameras. SEM-EDS analysis of the secondary craters showed evidence for residues only from the projectile and none from the mirror materials. Again, the ricochet material had speeds almost equal to the incidence particles and the angle of ricochet from the surface was close to 0°, i.e., they were scattered very close to the target surface. Numerical simulations of these results (Palmieri et al. 2003) showed that for incidence at 1°, the projectile ricochets intact (albeit with some plastic deformation), but that as impact angle increases fragmentation of the ricocheting projectile occurred at between 5° and 10°.

Taking the above experimental reports as a whole, we conclude that the amount of ejected material from a crater in a highly oblique impact is significantly less than from a normal incidence impact, but that it is still a finite fraction of the projectile mass. The projectile fragments can ricochet off the impact point with speed just under the initial impact speed and are concentrated in a forward cone raised above the target surface at a very shallow angle, whereas the bulk of the ejected target material is directed into certain zones and avoids others. The speed of the material is, however, very close to that of the original particle.

Clustering of impacts on a secondary surface can also occur for normal incidence penetration of thin sheets. The penetration disrupts the projectile into a cloud of fragments, combined with another cloud from displaced target material (e.g., Kipp and Grady 1995; Piekutowski et al. 1995). The cone of displaced target material has a relatively constant opening angle, while that of the disrupted projectile fragments is strongly dependent on absolute target thickness (Hörz et al. 1993). Depending on the relevant opening angles and the front sheet/secondary target separation, subsequent impacts on downstream targets can produce either clusters of hits, or a single broad, shallow crater with multiple pits within (Schultz and Gault 1983, 1985). However, in principle, there should be a mixture of the target and projectile materials in the central region of any impact site. The ratio of total displaced target to projectile material will depend on the relative thicknesses of the two (at high speeds and relatively thin targets, the whole area tends to the cross-sectional area of the projectile). However, this ratio can be lowered by the square of the relative opening angles of the two debris clouds. Nevertheless, since the two clouds overlap centrally, there should always be some amount of both materials in the center of any subsequent cluster of this. This changes if the original impact was on an inclined thin sheet, with the projectile material continuing in an approximately straight-through direction while the displaced target material is more normal to the rear of the target.

There is evidence for clustering of secondary craters from penetration of particles though Kapton on the Japanese Space Flyer Unit. This was retrieved from low Earth orbit in 1996. An examination (Graham et al. 2003) of the MLI blankets (uppermost layer was 50 μm thick Kapton) showed that small particle impact penetrations of the uppermost layer (50 mm thick Kapton) produced disruption of the impactors; in subsequent layers, a cluster of pits was typically observed. Debris in these pits included projectile and melted Kapton from the foils above, indicating an intermingling of the projectile and Kapton in the debris cloud, although it is not clear if this Kapton was from the front layer of the MLI or as a result of lower speed penetration of the subsequent layers.

Overall, both oblique impacts on thick surfaces or penetrations of thin layers can produce clusters of secondary hits. However, it is not clear how the penetration method can systematically change the direction of the projectile line of flight, and hence the angle made in the aerogel. In all the above discussions of laboratory experiments, competent, strong particles were used. What happens to weaker, more friable projectiles in oblique impacts needs to be demonstrated in the laboratory. We can, however, surmise that for shallow angle impacts instead of intact or large fragment ricochet effects, they may be more prone to fragmentation into their components.

SUMMARY

Here we summarize the observations, and review the evidence for and against all three scenarios that we have considered for explaining the impact clustering found on the Stardust aerogel and foil collectors.

Observations

1. There is statistically significant clustering of small tracks (maximum throat diameters ~100 μm) and small craters (maximum diameters <10 μm) on all length scales from microns to tens of centimeters. The evidence for

clustering among large tracks (>>100 μm) and craters (>10 μm) is statistically significant but weaker.
2. We observe off-normal tracks in aerogel tiles, distributed among normal-incidence tracks. These tracks display a systematically different morphology than normal-incidence tracks.
3. We observe a divergence of off-normal tracks between tiles 9 (many tracks) and 44 (two tracks) consistent with an origin on the central Whipple shield. The distribution of the intersection of track trajectories with the plane of the Whipple shield shows many tracks below −20 cm and no tracks above +20 cm. (0 cm is the projected center of the tray, and the positive direction is away from the spacecraft bus).
4. There is a large discrepancy in the spectral index and fluence at small particle sizes between the DFMI (PVDF detector) observations made during the cometary encounter and the crater observations made from the returned sample tray. Both crater and track analyses yield consistently fewer small particles than the DFMI. The DFMI observed two periods of dust collection, one centered on the closest approach time and another ~4000 km downrange of closest approach.
5. There is no evidence of spacecraft material in the impacts. It is not clear that this is a constraint because of the relative lack of relevant experimental data on the presence of forward-scattered target material in highly oblique impacts of small friable projectiles.
6. Electrostatic repulsion sets a seemingly hard lower limit of >>1 cm s^{-1} on the dispersion speed of disintegrating dust. This lower limit is based on straightforward physical principles.

Hypotheses

We have considered the following hypotheses:

- All impacts are primary, with a small radial velocity, and clustering occurs in the coma due to some unknown mechanism. This hypothesis is consistent with the observations of clustering and lack of spacecraft materials in impacts, but is not consistent with the presence of off-normal tracks, the expected large separation speeds expected for disintegrating dust in the cometary coma, nor the DFMI/crater discrepancy.
- All impacts are primary, with a large radial velocity, and clustering occurs in the coma due to some unknown mechanism. This hypothesis is consistent with the observations of clustering, lack of spacecraft materials in impacts, the presence of off-normal tracks, and could reconcile the DFMI data near closest approach with the cratering observations. This hypothesis is not consistent with the large separation speeds expected for disintegrating charged dust, nor with the DFMI data at ~11 min after closest approach.
- Large impacts are primary, but there is a population of small grains due to at least one impact on the central Whipple shield. This appears to be consistent with all the observations, with the exception of the discrepancy between the cratering and DFMI measurements of dust fluences, the marginally significant clustering observed in both $\hat{\xi}_1$ and $\hat{\zeta}$ for large (>300 μm) tracks, and (possibly) the lack of spacecraft materials in impacts.

Although no hypothesis explains all observations, we conclude that the preponderance of evidence points to an impact on the central Whipple shield as the origin of both off-normal tracks and clustering. To be sure, none of the scenarios have been completely ruled out—it is even possible that all three mechanisms operate. Nevertheless, it is clear that researchers should be aware of the possibility that tracks, particularly off-normal tracks, may have been "pre-processed" before capture by a collision with the central Whipple shield, and should be vigilant to contamination from the spacecraft.

Acknowledgments—We thank the entire Stardust Team—dedicated and talented people, too numerous to acknowledge individually here, whose intense effort over many years culminated in the successful recovery of the Stardust capsule in January 2006 bearing the first solid samples returned from beyond the Moon. We especially thank Steven Jones for synthesis of aerogel tiles.

A. J. W. and several other co-authors were supported by a NASA Stardust Participating Scientist grant. S. A. S. is grateful for support from the Stardust Project. This work was in part performed under the auspices of the U.S. Department of Energy, National Nuclear Security Administration by the University of California, Lawrence Livermore National Laboratory under contract no. W-7405-Eng-48. The work at LLNL was supported by NASA grants NAG5-10696, NNH04AB49I and NNH06AD67I.

Editorial Handling—Dr. A. J. Timothy Jull

REFERENCES

Anderson J. L. B., Schultz P. H., and Heineck J. T. 2003. Asymmetry of ejecta flow during oblique impacts using three-dimensional particle image velocimetry. *Journal of Geophysical Research* 109, doi:10.1029/2003JE002075.

Brownlee D. E., Hörz F., Newburn R. L., Zolensky M., Duxbury T. C., Sandford S., Sekanina Z., Tsou P., Hanner M. S., Clark B. C., Green S. F., and Kissel J. 2004. Surface of young Jupiter-family comet 81 P/Wild 2: View from the Stardust spacecraft. *Science* 304:1764–1769.

Burchell M. J. and Mackay N. 1998. Crater ellipticity in hypervelocity impact on metals. *Journal of Geophysical Research* 103:22,761–22,774.

Burchell M .J. and Whitehorn L. 2003. Oblique incidence hypervelocity impacts on rock. *Monthly Notices of the Royal Astronomical Society* 341:192–198.

Burchell M. J., Fairey S., Wozniakeiwicz P., Brownlee D., Hörz F., Kearsley A., Westphal A. J., Green S., Trigo-Rodríguez J., and See T. 2008. Characteristics of cometary dust tracks in Stardust aerogel and laboratory calibrations. *Meteoritics and Planetary Science* 43. This issue.

Clark B. C., Green S. F., Economou T. E., Sandford S. A., Zolensky M. E., McBride N., and Brownlee D. E. 2004. Release and fragmentation of aggregates to produce heterogeneous, lumpy coma streams. *Journal of Geophysical Research* 109, doi: 10.1029/2004JE002319.

Davis M. and Peebles P. J. E. 1983. A survey of galaxy redshifts. V—The two-point position and velocity correlations. *The Astrophysical Journal* 267:465–482.

Drolshagen G., McDonnell J. A. M., Stevenson T. J., Deshpande S., Kay L., Tanner W. G., Mandeville J. C., Carey W. C., Maag C. R., Griffiths A. D., Shrine N. G., and Aceti R. 1996. Optical survey of micrometeoroid and space debris impact features on EURECA. *Planetary and Space Science* 44:317–340.

Farnham T. L. and Schleicher D. G. 2005. Physical and compositional studies of comet 81P/Wild 2 at multiple apparitions. *Icarus* 173:533–558.

Flynn G. J., Bleuet P., Borg J., Bradley J. P., Brenker F. E., Brennan S., Bridges J., Brownlee D. E., Bullock E. S., Burghammer M., Clark B. C., Dai Z. R., Daghlian C. P., Djouadi Z., Fakra S., Ferroir T., Floss C., Franchi I. A., Gainsforth Z., Gallien J.-P., Gillet Ph., Grant P. G., Graham G. A., Green S. F., Grossemy F., Heck P. R., Herzog G. F., Hoppe P., Hörz F., Huth J., Ignatyev K., Ishii H. A., Janssens K., Joswiak D., Kearsley A. T., Khodja H., Lanzirotti A., Leitner J., Lemelle L., Leroux H., Luening K., MacPherson G. J., Marhas K. K., Marcus M. A., Matrajt G., Nakamura T., Nakamura-Messenger K., Nakano T., Newville M., Papanastassiou D. A., Pianetta P., Rao W., Riekel C., Rietmeijer F. J. M., Rost D., Schwandt C. S., See T. H., Sheffield-Parker J., Simionovici A., Sitnitsky I., Snead C. J., Stadermann F. J., Stephan T., Stroud R. M., Susini J., Suzuki Y., Sutton S. R., Taylor S., Teslich N., Troadec D., Tsou P., Tsuchiyama A., Uesugi K., Vekemans B., Vicenzi E. P., Vincze L., Westphal A. J., Wozniakiewicz P., Zinner E., and Zolensky M. E. 2006. Elemental compositions of comet 81P/Wild 2 samples collected by Stardust. *Science* 314: 1731–1735.

Gault D. E. 1973. Displaced mass, depth, diameter, and effects of oblique trajectories for impact craters formed in dense crystalline rocks. *The Moon* 6:32–44.

Gault D. E. and Schultz P. H. 1986. Oblique impact: Projectile ricochet, concomitant ejecta, and momentum transfer. *Meteoritics* 21:368–369.

Gault D. E. and Wedekind J. A. 1978. Experimental studies of oblique impact. Proceedings, 9th Lunar and Planetary Science Conference. pp. 3843–3875.

Gehrels N. 1986. Confidence limits for small numbers of events in astrophysical data. *The Astrophysical Journal* 303:336–346.

Graham G. A., Kearsley A. T., Wright I. P., Burchell M. J., and Taylor E. A. 2003. Observations on hypervelocity impact damage sustained by multi-layered insulation foils exposed in low Earth orbit and simulated in the laboratory. *International Journal of Impact Engineering* 29:307–316.

Green S. F., McDonnell J. A. M., McBride N., Colwell M. T. S. H., Tuzzolino A. J., Economou T. E., Tsou P., Clark B. C., and Brownlee D. E. 2004. The dust mass distribution of comet 81P/Wild 2. *Journal of Geophysical Research-Planets* E12, 109:S04.

Horányi M. 1996. Charged dust dynamics in the Solar System. *Annual Review of Astronomy and Astrophysics* 34:383–418.

Horányi M. and Goertz C. K. 1990. Coagulation of dust particles in a plasma. *The Astrophysical Journal* 361:155–161.

Hörz F., Cintala M. J., Bernhard R. P., and See T. H. 1993. Dimensionally scaled penetration experiments to extract projectile sizes from space exposed surfaces. *International Journal of Impact Engineering* 14:347–358.

Hörz F., Bastien R., Borg J., Bradley J. P., Bridges J. C., Brownlee D. E., Burchell M. J., Chi M., Cintala M. J., Dai Z. R., Djouadi Z., Dominguez G., Economou T. E., Fairey S. A. J., Floss C., Franchi I. A., Graham G. A., Green S. F., Heck P., Hoppe P., Huth J., Ishii H., Kearsley A. T., Kissel J., Leitner J., Leroux H., Marhas K., Messenger K., Schwandt C. S., See T. H., Snead C., Stadermann F. J., Stephan T., Stroud R., Teslich N., Trigo-Rodríguez J. M., Tuzzolino A. J., Troadec D., Tsou P., Warren J., Westphal A., Wozniakiewicz P., Wright I., and Zinner E. 2006. Impact features on Stardust: Implications for comet 81P/Wild 2 dust. *Science* 314:1716–1719.

Kearsley A. T., Borg J., Graham G. A., Burchell M. J., Cole M. J., Leroux H., Bridges J. C., Hörz F., Wozniakiewicz P. J., Bland P. A., Bradley J. P., Dai Z. R., Teslich N., See T., Hoppe P., Heck P. R., Huth J., Stadermann F. J., Floss C., Marhas K., Stephan T., and Leitner J. 2008. Dust from comet Wild 2: Interpreting particle size, shape, structure, and composition from impact features on the Stardust aluminum foils. *Meteoritics & Planetary Science* 43. This issue.

Kipp M. E. and Grady D. E. 1995. Experimental and numerical studies of high-velocity impact fragmentation. In *High-pressure shock compression of solids II*, edited by Davison L., Grady D. E., and Shahinpoor M. New York: Springer. pp. 283–339.

Leitner J., Stephan T., Kearsley A. T., Hörz F., Flynn G. J., and Sandford S. A. 2008. TOF-SIMS analysis of crater residues from Wild 2 cometary on Stardust aluminum foil. *Meteoritics & Planetary Science* 43. This issue.

Levine A. S., editor. 1993. *LDEF—69 months in space*. Washington, D.C.: National Aeronautics and Space Administration. 561 p.

Meidinger N., Aschenbach B., Brauninger H., Drolshagen G., Englhauser J., Hartmann R., Hartner G., Srama R., Struder L., Stubig M., and Trumper J. 2003. Experimental verification of a micrometeoroid damage in the PN-CCD camera system aboard XMM-Newton. In *X-ray and gamma-ray telescopes and instruments for astronomy*, edited by Truemper J. E. and Tananbaum H. D. Bellingham, Washington: SPIE. pp. 243–254.

Mendis D. A. and Rosenberg M. 1994. Cosmic dusty plasma. *Annual Review of Astronomy and Astrophysics* 32:419–463.

Palmieri D., Drolshagen G., and Lambert M. 2003. Numerical simulation of grazing impacts from micron-sized particles on the XMM-Newton mirrors. *International Journal of Impact Engineering* 29:527–536.

Piekutowski A. J. 1995. Radiographic studies of impact fragmentation. In *High-pressure shock compression of solids II*, edited by Davison L., Grady D. E., and Shahinpoor M. New York: Springer. pp. 150–175.

Rival M. and Mandeville J. C. 1999. Modelling of ejecta produced upon hypervelocity impacts. *Space Debris* 1:45–57.

Sandford S. A., Aléon J., Alexander C. M. O'D., Araki T., Bajt S., Baratta G. A., Borg J., Bradley J. P., Brownlee D. E., Brucato J. R., Burchell M. J., Busemann H., Butterworth A., Clemett S. J., Cody G., Colangeli L., Cooper G., D'Hendecourt L., Djouadi Z., Dworkin J. P., Ferrini G., Fleckenstein H., Flynn G. J., Franchi I. A., Fries M., Gilles M. K., Glavin D. P., Gounelle M., Grossemy F., Jacobsen C., Keller L. P., Kilcoyne A. L. D., Leitner J., Matrajt G., Meibom A., Mennella V., Mostefaoui S., Nittler L. R., Palumbo M. E., Papanastassiou D. A., Robert F., Rotundi A., Snead C. J., Spencer M. K., Stadermann F. J., Steele A., Stephan T., Tsou P., Tyliszczak T., Westphal A. J., Wirick S., Wopenka B., Yabuta H., Zare R. N., and Zolensky M. E.

2006. Organics captured from comet 81P/Wild 2 by the Stardust spacecraft. *Science* 314:1720–1724.

Schultz P. H. and Gault D. E. 1983. High-velocity clustered impacts: Experiments and implications. *Journal of Geophysical Research* 90:3701–3732.

Schultz P. H. and Gault D. E. 1985. Clustered impacts: Experimental results (abstract). 14th Lunar and Planetary Science Conference. p. 674.

Schultz P. H. and Gault D. E. 1990. Prolonged global catastrophes from oblique impact. In *Global catastrophes in Earth history*, edited by Sharpton V. L. and Ward P. D. GSA Special Paper #247. Boulder, Colorado: Geological Society of America. pp. 239–261.

Sekanina Z., Brownlee D. E., Economou T. E., Tuzzolino A. J., and Green S. F. 2004. Modeling the nucleus and jets of comet 81P/Wild 2 based on the Stardust encounter data. *Science* 304:1769–1774.

Simpson J. C., Simons S., and Williams I. P. 1979. Thermal coagulation of charged grains in dense clouds. *Astrophysics and Space Science* 61:65–80.

Squyres S. W., Howell C., Liu M. C., and Lissauer J. J. 1997. Investigation of crater "saturation" using spatial statistics. *Icarus* 125:67–82.

Tsou P., Brownlee D. E., Sandford, S. A., Hörz, F., and Zolensky. M. E. 2003. Wild 2 and interstellar sample collection and Earth return. *Journal of Geophysical Research* 108, doi:10.1029/2003JE002109.

Tuzzolino A. T. Economou T. E., McKibben R. B., Simpson J. A., McDonnell J. A. M., Burchell M. J., Vaughan B. A. M., Tsou P., Hanner M. S., Clark B. C., and Brownlee D. E. Dust Flux Monitor Instrument for the Stardust mission to comet Wild 2. 2003. *Journal of Geophysical Research* 108, doi:10.1029/2003JE002086.

Tuzzolino A. J., Economou, T. E., Clark B. C., Tsou P., Brownlee D. E., Green S. F., McDonnell J. A. M., McBride N., and Colwell M. T. S. H. Dust measurements in the coma of comet 81P/Wild 2 by the Dust Flux Monitor Instrument. *Science* 304:1776–1780.

Yelle R. V., Soderblom, L. A., and Jokipii J. R. 2003. Formation of jets in Comet 19P/Borrelly by subsurface geysers. *Icarus* 167: 30–36.

Zolensky M. E., Zega T. J., Yano H., Wirick S., Westphal A. J., Weisberg M. K., Weber I., Warren J. L., Velbel M. A., Tsuchiyama A., Tsou P., Toppani A., Tomioka N., Tomeoka K., Teslich N., Taheri M., Susini J., Stroud R., Stephan T., Stadermann F. J., Snead C. J., Simon S. B., Simionovici A., See T. H., Robert F., Rietmeijer F. J. M., Rao W., Perronnet M. C., Papanastassiou D. A., Okudaira K., Ohsumi K., Ohnishi I., Nakamura-Messenger K., Nakamura T., Mostefaoui S., Mikouchi T., Meibom A., Matrajt G., Marcus M. A., Leroux H., Lemelle L., Le L., Lanzirotti A., Langenhorst F., Krot A. N., Keller L. P., Kearsley A. T., Joswiak D., Jacob D., Ishii H., Harvey R., Hagiya K., Grossman L., Grossman J. N., Graham G. A., Gounelle M., Gillet Ph., Genge M. J., Flynn G., Ferroir T., Fallon S., Ebel D. S., Dai Z. R., Cordier P., Clark B., Chi M., Butterworth A. L., Brownlee D. E., Bridges J. C., Brennan S., Brearley A., Bradley J. P., Bleuet P., Bland P. A., and Bastien R. 2006. Mineralogy and petrology of comet 81P/Wild 2 nucleus samples. *Science* 314:1735–1739.